

# Hurricane Bonnie (1998): Maintaining Intensity during High Vertical Wind Shear and an Eyewall Replacement Cycle

ERIN M. DOUGHERTY

*Department of Atmospheric Science, Colorado State University, Fort Collins, Colorado*

JOHN MOLINARI

*Department of Atmospheric and Environmental Sciences, University at Albany, State University of New York, Albany, New York*

ROBERT F. ROGERS AND JUN A. ZHANG

*Hurricane Research Division, NOAA/Atlantic Oceanographic and Meteorological Laboratory, Miami, Florida*

JAMES P. KOSSIN

*NOAA/National Centers for Environmental Information, Madison, Wisconsin*

(Manuscript received 23 January 2018, in final form 7 August 2018)

## ABSTRACT

Hurricane Bonnie (1998) was an unusually resilient hurricane that maintained a steady-state intensity while experiencing strong ( $12\text{--}16\text{ m s}^{-1}$ ) vertical wind shear and an eyewall replacement cycle. This remarkable behavior was examined using observations from flight-level data, microwave imagery, radar, and dropsondes over the 2-day period encompassing these events. Similar to other observed eyewall replacement cycles, Bonnie exhibited the development, strengthening, and dominance of a secondary eyewall while a primary eyewall decayed. However, Bonnie's structure was highly asymmetric because of the large vertical wind shear, in contrast to the more symmetric structures observed in other hurricanes undergoing eyewall replacement cycles. It is hypothesized that the unusual nature of Bonnie's evolution arose as a result of an increase in vertical wind shear from  $2$  to  $12\text{ m s}^{-1}$  even as the storm intensified to a major hurricane in the presence of high ambient sea surface temperatures. These circumstances allowed for the development of outer rainbands with intense convection downshear, where the formation of the outer eyewall commenced. In addition, the circulation broadened considerably during this time. The secondary eyewall developed within a well-defined beta skirt in the radial velocity profile, consistent with an earlier theory. Despite the large ambient vertical wind shear, the outer eyewall steadily extended upshear, supported by 35% larger surface wind speed upshear than downshear. The larger radius of maximum winds during and after the eyewall replacement cycle might have aided Bonnie's resiliency directly, but also increased the likelihood that diabatic heating would fall inside the radius of maximum winds.

## 1. Introduction

Prediction of tropical cyclone (TC) intensity remains a challenging problem, as evidenced by little improvement in accuracy since the 1990s (Rappaport et al. 2009). A myriad of factors complicates this issue, as both internal dynamics and external forcings affect storm intensity. Two particularly well-cited influences on TC intensity change include vertical wind shear (e.g., Simpson and

Riehl 1958; DeMaria 1996; Frank and Ritchie 2001; Riemer et al. 2010; Tang and Emanuel 2010) and eyewall replacement cycles (ERCs; e.g., Willoughby et al. 1982; Houze et al. 2007; Sitkowski et al. 2011, hereafter S11; Kossin and DeMaria 2016).

Vertical wind shear is known to typically weaken TCs as well as modify their structure. Various pathways have been proposed by which shear-induced weakening occurs, such as forced subsidence at midlevels upshear over the storm center (DeMaria 1996), erosion of the upper-level warm core (Frank and Ritchie 2001), and ventilation of the TC core with midlevel dry air by

---

*Corresponding author:* Erin M. Dougherty, edough@rams.colostate.edu

eddies (Tang and Emanuel 2010). Riemer et al. (2010) additionally suggested that TCs weaken through shear-induced downdrafts that flush low equivalent potential temperature into the boundary layer. These downdrafts proposed by Riemer et al. (2010) emanated from a shear-induced asymmetric convective structure reminiscent of a stationary band complex (Willoughby et al. 1984). Such shear-induced asymmetries were observed by Corbosiero and Molinari (2002), who found that deep convection preferentially occurred downshear in TCs. This relationship was stronger in higher shear and for more intense storms (but only in the inner core; Corbosiero and Molinari 2002). Composite analysis of thousands of dropsonde data collected in 13 hurricanes confirmed the asymmetric distribution of boundary layer equivalent potential temperature in relationship to shear (Zhang et al. 2013).

Despite the well-documented relationship between vertical shear and TC weakening, TCs do not always weaken in high shear. A number of observational studies noted TC intensification despite strong shear, as intense convection developed within the radius of maximum winds (Shelton and Molinari 2009; Molinari and Vollaro 2010; Nguyen and Molinari 2012). Though asymmetric in nature, this convection was strong enough to increase the azimuthally averaged diabatic heating that aided intensification (Molinari and Vollaro 2010; Nguyen and Molinari 2012). The observed convective structures furthermore evolved with vortex tilt, during which the inner vortex (the inner core; i.e., inside the radius of maximum winds) remained more upright than the tilted outer vortex (the outer core; i.e., beyond the radius of maximum winds), as observed by the displacement of the zero isodop (i.e., zero radial velocity) position (Molinari and Vollaro 2010; Nguyen and Molinari 2012).

The evolution of vortex tilt is another mechanism that has been proposed by which TCs resist shear. A left-of-shear tilt configuration, such as that seen in Hurricane Guillermo (1997; Reasor and Eastin 2012), is considered favorable for a sheared TC since it minimizes the net vertical shear. Additionally, a vortex can resist shear by realigning itself through the precession of upper- and lower-level vortex centers (Jones 1995) or by a vortex Rossby wave damping mechanism (Reasor et al. 2004).

ERCs also produce substantial intensity changes in TCs. In their seminal study, Willoughby et al. (1982) observed TC weakening as an outer convective ring contracted and intensified around a decaying inner eyewall. Once the inner eyewall vanished and the outer eyewall replaced it, the hurricane reintensified (Willoughby et al. 1982). S11 further detailed the stages of ERCs in their climatological study of North Atlantic hurricanes. The three expected stages of intensity changes associated with ERCs are as follows: 1) intensification, during which an inner wind

maximum reaches its peak intensity while an outer wind maximum associated with rainbands first appears; 2) weakening, during which the inner wind maximum weakens while the outer wind maximum contracts and intensifies, forming a concentric eyewall; and 3) reintensification, during which the outer wind maximum's intensity exceeds that of the inner, as the inner one decays and vanishes (S11).

ERCs and secondary eyewall formation (SEF) are frequently observed in hurricanes, but no formal definition of these processes exists in the literature. For the purposes of this paper, the time of SEF will refer to the first appearance of an outer wind maximum in the symmetric tangential velocity. The term ERC will refer to the completion of the cycle (i.e., loss of the inner wind maximum and establishment of the outer as the sole maximum).

Despite the common occurrence of ERCs and SEF in hurricanes (Hawkins et al. 2006), their cause is still relatively unknown. Nong and Emanuel (2003) suggested that a sufficiently strong external forcing, such as an upper-level trough, is necessary for SEF. Many other studies point to the importance of internal processes in producing a secondary eyewall. Vortex Rossby waves are one such mechanism that can accelerate the mean tangential wind at some radius from the center of the vortex through wave-mean flow interactions (Montgomery and Kallenbach 1997). This occurs through the outward propagation of waves on a negative radial vorticity gradient and eventual stagnation at about 3 times the radius of maximum winds. The importance of the axisymmetric vorticity structure in SEF was highlighted in Terwey and Montgomery's (2008) beta-skirt hypothesis, in which convectively generated vorticity occurring in a region of a gentle negative radial vorticity gradient (beta skirt) can transfer energy into the mean flow. Additional hypotheses suggest that unbalanced boundary layer dynamics are sufficient for SEF (Huang et al. 2012; Abarca and Montgomery 2013, 2015). It is feasible that both external conditions and internal storm dynamics are important to SEF, as suggested by Kossin and DeMaria (2016) and Kossin and Sitkowski (2009).

Findings from Kossin and Sitkowski (2009) show that SEF occurs, on average, in moderate (e.g.,  $6 \text{ m s}^{-1}$ ) shear. Didlake and Houze (2011) described a low shear ERC event in Hurricane Rita (2005), in which the ERC was primarily examined from a symmetric viewpoint. In contrast, vertical shear (and thus asymmetric) impacts on ERCs have not been examined until recently. In a case study of Hurricane Gonzalo, Didlake et al. (2017) observed asymmetric eyewalls with respect to moderate ( $4\text{--}7 \text{ m s}^{-1}$ ) shear. The differing asymmetries between the primary and secondary eyewalls in Gonzalo were hypothesized to be the result of tilt and interaction with a stationary band complex (Didlake et al. 2017). However,

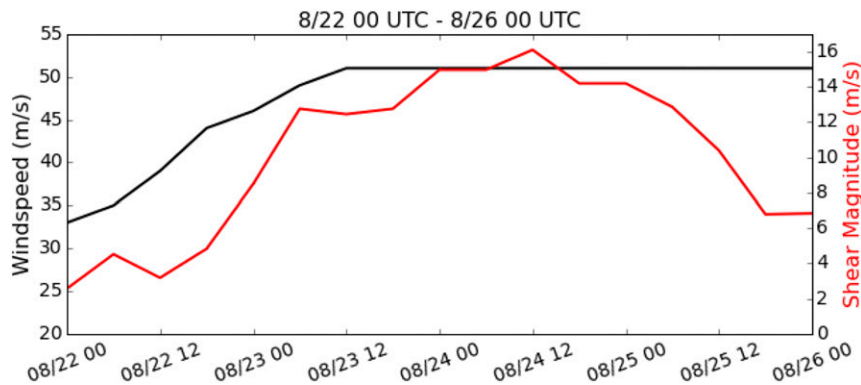


FIG. 1. Bonnie's maximum wind speed ( $\text{m s}^{-1}$ ; black line and left y axis) and 850–200-hPa shear magnitude ( $\text{m s}^{-1}$ ; red line and right y axis) from 0000 UTC 22 Aug to 0000 UTC 26 Aug. Wind speed was obtained from the Extended Best Track Dataset and shear magnitude was obtained from the Statistical Hurricane Intensity Prediction Scheme (SHIPS) dataset.

Didlake et al. (2017) did not speculate about the role of shear in the development of Gonzalo's ERCs. This question was instead addressed in SEF simulations performed by Dai et al. (2017) and Zhang et al. (2017). In Dai et al.'s (2017) simulation, eddy flux convergence from a midlatitude jet produced an asymmetric stratiform cloud from which a secondary eyewall formed. Zhang et al.'s (2017) study similarly suggested that moderate environmental wind shear provided forcing for outer rainbands to develop and a secondary eyewall to form from the rainbands. Results from Dai et al. (2017) and Zhang et al. (2017) generally support Nong and Emanuel's (2003) idea that a strong external forcing can trigger a secondary eyewall. These results suggest that the link between environmental influences and SEF is an important one.

Though these previous studies examined various aspects of vertical wind shear and ERCs, none have conducted a detailed case study of an ERC in a highly sheared, steady-state storm, as was the case in Hurricane Bonnie (1998). Shear in Bonnie was nearly double that of Hurricane Gonzalo (Didlake et al. 2017) and far exceeded the range of shear usually encountered by hurricanes undergoing ERCs (Kossin and Sitkowski 2009). The objectives of this study are to document the evolution of symmetric and asymmetric aspects of Bonnie's ERC, compare these results with other ERCs, and understand how Bonnie remained steady state during its ERC and strong shear. This will be accomplished through use of radar, flight-level data, microwave imagery, and dropsondes in Bonnie from 23 to 25 August 1998.

## 2. Bonnie's storm history

The complete evolution of Hurricane Bonnie is documented in Rogers et al. (2003) and Zhu et al. (2004). Early in its life cycle as a hurricane, Bonnie rapidly

intensified from 0000 UTC 22 August to 1200 UTC 23 August (Fig. 1). Bonnie was unusual even during its rapid intensification phase, which occurred despite an increase in vertical wind shear from 2 to  $12 \text{ m s}^{-1}$ . This increase in shear was due to Bonnie's proximity to an upper-level trough over the southeastern United States (Braun et al. 2006). From 1200 UTC 23 August to 0000 UTC 25 August, shear continued to increase to over  $14 \text{ m s}^{-1}$  while Bonnie maintained a constant  $51 \text{ m s}^{-1}$  intensity. After 0000 UTC 25 August, shear diminished to  $7 \text{ m s}^{-1}$  by 1800 UTC August 25 and Bonnie continued to maintain its intensity.

Prior studies suggested that increasingly warm ( $28^{\circ}$ – $30.5^{\circ}\text{C}$ ) sea surface temperatures (SSTs) may have contributed to Bonnie's intensification and resiliency in high shear (Heysmsfield et al. 2001; Molinari and Vollaro 2008). These Reynolds SST values were obtained a week prior at a resolution of 100 km (Wentz et al. 2000). Observations therefore suggest that warm waters preceded Bonnie's passage, but the influence of SSTs later in Bonnie's life is not as clear (see section 5d).

Two observational studies and four modeling studies examined shear-related impacts on Bonnie's evolution [see Molinari and Vollaro (2008) for a complete review of these studies]. Heysmsfield et al. (2001) noted the presence of convective bursts in Bonnie's eyewall during the intensification period from 1800 UTC 21 August to 23 August. After this intensification period, Zhu et al.'s (2004) simulation exhibited a secondary eyewall at 0000 UTC 24 August during a period of high vertical wind shear. However, because of a shear-induced asymmetric structure, Zhu et al. (2004) chose to focus on a more axisymmetric ERC that occurred at approximately 0000 UTC 26 August.

The SEF (ERC) at 0000 UTC 24 August (1200 UTC 24 August) is of particular interest in this study.

In addition to maintaining resiliency in the face of high vertical wind shear, the occurrence of an ERC in Bonnie further deviates from the expected behavior of a strongly sheared TC. It is this unusual lack of intensity change in Bonnie that motivates this study.

### 3. Data and methods

#### a. Flight-level data

Data obtained from eight different flights from 23 to 25 August were utilized in this study (Table 1). Aircraft reconnaissance missions by the U.S. Air Force (USAF) WC-130 and the National Oceanic and Atmospheric Administration (NOAA) WP-3D N42RF and N34RF (P-3) collected nearly continuous 1-Hz frequency measurements of temperature  $T$ , dewpoint temperature  $T_d$ , and wind at 700 and 600 hPa, respectively. The NOAA P-3 aircraft additionally measured vertical velocity  $w$  and reflectivity from the lower fuselage (LF) and tail (TA) Doppler radar. Aircraft data were transformed into storm-relative coordinates following Willoughby and Chelmon's (1982) center-position determination method, and then interpolated into 0.5-km bins along a 150-km radial leg.

Additional quantities calculated from the flight-level data include the symmetric component of relative vorticity  $\zeta$  and absolute angular momentum  $m_a$ , given by

$$\bar{\zeta} = \frac{\partial \bar{v}}{\partial r} + \frac{\bar{v}}{r}, \quad (1)$$

$$\bar{m}_a = r\bar{v} + \frac{fr^2}{2}. \quad (2)$$

A centered finite-difference approximation was used to calculate  $\zeta$  in Eq. (1). These quantities, along with wind, were fit with a 10th-order polynomial to isolate major structural changes and minimize local fluctuations (Figs. 2–5).

Radius versus time Hovmöllers were created using USAF (700 hPa) flight data to understand the evolution of axisymmetric quantities (horizontal wind and  $m_a$ ). Flight legs from four different flights (i.e., flights A1–A4) were placed into nine 6-hourly time bins. This resulted in six to nine flight legs in five of the time bins (1200–1800 UTC 23–25 August and 0000–0600 UTC 24 and 25 August) and one to two legs in the remaining four time bins. Flight legs were averaged together in each time bin to provide ample azimuthal coverage, except for time bins consisting of only one to two legs, for which linear interpolations of the previous and subsequent 6-h time bins were taken. Hovmöller plots display the midpoint of each time bin (i.e., at hour 3).

TABLE 1. Description of flight-level data used in this study of Hurricane Bonnie (1998) from 23 to 25 Aug. Flights A1–A4 refer to USAF C-130 flights, while flights P1–P4 refer to NOAA P-3 flights. “No. of passes” refers to the number of center passes in each flight, “No. of drops” refers to the number of dropsondes dropped, and LF (TA) stands for lower-fuselage (tail) radar, respectively. See text for details.

Flight	No. of passes	Pressure (hPa)	Start time	End time	Midtime	No. of drops	LF	TA	Dual Doppler
A1	6	700	0813 UTC 23 Aug	1733 UTC 23 Aug	1200 UTC 23 Aug	6	No	No	No
A2	10	700	1956 UTC 23 Aug	0718 UTC 24 Aug	0000 UTC 24 Aug	7	No	No	No
P1	8	600	1736 UTC 23 Aug	0230 UTC 24 Aug	0000 UTC 24 Aug	24	Yes	FAST and normal	No
P2	4	600	1726 UTC 23 Aug	0240 UTC 24 Aug	0000 UTC 24 Aug	—	Yes	Normal	No
A3	8	700	0757 UTC 24 Aug	1848 UTC 24 Aug	1200 UTC 24 Aug	7	No	No	No
A4	10	700	1951 UTC 24 Aug	0643 UTC 25 Aug	0000 UTC 25 Aug	6	No	No	No
P3	10	600	1834 UTC 24 Aug	0200 UTC 25 Aug	0000 UTC 25 Aug	19	Yes	Normal	Yes
P4	10	850	1825 UTC 24 Aug	0310 UTC 25 Aug	0000 UTC 25 Aug	—	Yes	FAST	Yes

### b. Radar data

The LF and TA radars aboard the NOAA WP-3D aircraft collected data during flights P1, P2, P3, and P4 (Table 1). The LF is a C-band horizontal polarization radar that scans azimuthally from its location at the base of the plane. The TA radar is an X-band vertical polarization radar located in the plane's tail (Jorgensen 1984), which can be operated in two scanning modes: normal and fore/aft scanning technique (F/AST; Gamache and Marks 1995). Both TA radar scanning modes operated during flight P1, while flights P2 and P3 operated in normal mode, and flight P4 operated exclusively in F/AST mode (Table 1).

While the LF radar solely provides flight-level reflectivity data, additional information was gleaned through processing the TA radar reflectivity and Doppler velocity data using Gamache's (1997) automated variational algorithm. Solving the radar projection equations and continuity equation, solutions from Gamache's (1997) algorithm produced a three-dimensional gridded (swath) analysis during flight P1 with a  $2 \times 2 \text{ km}^2$  horizontal and 0.5-km vertical resolution over a  $400 \times 400 \text{ km}^2$  domain size (Reasor et al. 2009; Rogers et al. 2015). These swaths were analyzed out to 150 km in radius and up to 18 km in height. In the swath analyses, data included vertical and horizontal winds and reflectivity (Rogers et al. 2012).

Additionally, 3D winds from the TA radar allowed for Bonnie's tilt to be estimated. Tilt was estimated by the displacement of the circulation center of Earth-relative winds and minimum wind speed at 2-, 5-, 8-, and 11-km altitude during P1 centered at 0000 UTC 24 August. Because of a lack of scatterers in small areas in Bonnie's center, however, some uncertainty exists in this tilt estimate. Despite this uncertainty, a qualitative assessment of the tilt direction and magnitude relative to the vertical shear vector was performed.

### c. Dropsondes

From 0800 UTC 23 August to 0200 UTC 25 August, the USAF C-130, NOAA WP-3D, and NASA DC-8 aircraft released 71 dropsondes within 150 km of the center in Hurricane Bonnie. Dropsondes measured  $T$ ,  $T_d$ ,  $w$ , and horizontal winds from flight level (600 or 700 hPa, depending on the aircraft) to the sea surface and were interpolated to 100-m spacing in the vertical. Using Willoughby and Chelmon's (1982) storm center detection method, storm motion and sonde drift were removed so dropsonde data are storm relative. A majority of the dropsondes sampled late on 23 and 24 August when all four aircraft were flying, with sparser dropsonde observations earlier on both days (Table 1). Dropsondes were utilized to create composites in the secondary eyewall region (70–100 km) during SEF (2000 UTC 23 August–0021 UTC

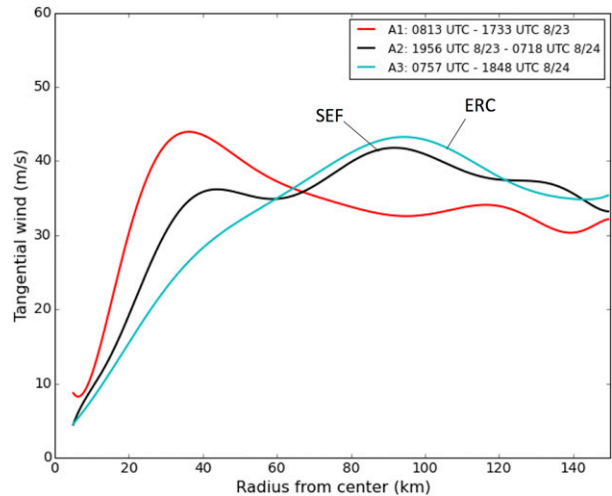


FIG. 2. Axisymmetric tangential wind for three separate U.S. Air Force (700 hPa) flights: 0813–1733 UTC 23 Aug (flight A1, red), 1956 UTC 23 Aug–0718 UTC 24 Aug (flight A2, black), and 0757–1848 UTC 24 Aug (flight A3, blue). Flight A2 (A3) is labeled SEF (ERC) to denote when secondary eyewall formation occurred (the eyewall replacement cycle completed). A total of 6–10 radial legs were averaged for each flight to obtain an axisymmetric quantity.

24 August) and for the entire observation period (1200 UTC 23 August–0000 UTC 25 August).

### d. Additional data

Vertical wind shear data available every 6 hours were obtained from the Statistical Hurricane Intensity Prediction Scheme (SHIPS). Shear is calculated in SHIPS as the magnitude difference between 850- and 200-hPa wind vectors, averaged over a 200–800-km radius from the vortex center (DeMaria et al. 2005).

Additional TC environmental parameters and storm intensity data were obtained from SHIPS. A total of 82 different variables taken from the SHIPS dataset were fed into Kossin and Sitkowski's (2009) ERC prediction model, which covered a time period from 1997 to 2006 and included 45 SEF events (Kossin and Sitkowski 2009) among North Atlantic hurricanes. Statistics of these features for SEF events and nonevents were compared with those of Hurricane Bonnie to better place Bonnie's ERC in context with other TCs undergoing an ERC.

## 4. Bonnie's eyewall replacement cycle

### a. Symmetric ERC evolution

Radial profiles of tangential wind  $\bar{v}$  and  $\bar{\zeta}$  obtained from three consecutive USAF flights from 23 to 24 August capture three distinct stages in Bonnie's ERC. During flight A1 (Fig. 2), a single  $\bar{v}_{\max}$  of  $45 \text{ m s}^{-1}$  was located

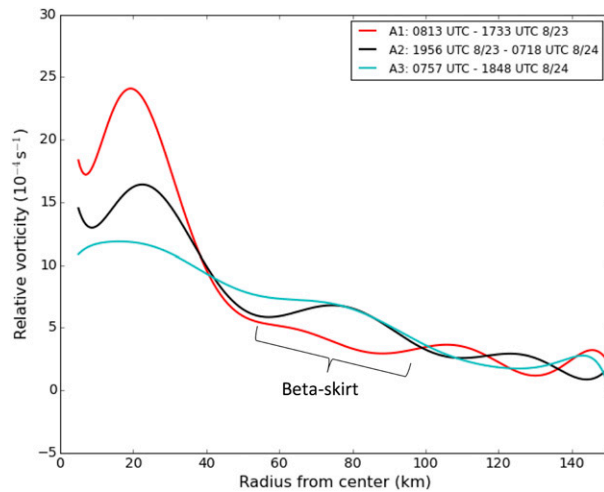


FIG. 3. As in Fig. 2, but for relative vorticity ( $\times 10^{-4} \text{ s}^{-1}$ ). The gentle negative radial gradient in relative vorticity during flight A1 is denoted as the beta skirt.

at a radius of 35 km, outside of which winds gradually decreased. By flight A2, a double  $\bar{v}_{\text{max}}$  was present, as a secondary  $\bar{v}_{\text{max}}$  of  $42 \text{ m s}^{-1}$  formed and intensified at the 90-km radius. This secondary  $\bar{v}_{\text{max}}$  in flight A2 was nearly the same intensity of the primary  $\bar{v}_{\text{max}}$  from flight A1, confirming Bonnie's steady-state intensity from Fig. 1. Concurrently, the primary  $\bar{v}_{\text{max}}$  weakened to  $35 \text{ m s}^{-1}$ . In flight A3, the primary  $\bar{v}_{\text{max}}$  disappeared and the secondary  $\bar{v}_{\text{max}}$  became the only  $\bar{v}_{\text{max}}$ . The series of events shown in Fig. 2 is typical for ERC events (Willoughby et al. 1982; S11; Didlake et al. 2017), except for the lack of secondary  $\bar{v}_{\text{max}}$  contraction during and after flight A2.

Accompanying changes in  $\bar{v}$  during Bonnie's ERC were changes in axisymmetric relative vorticity  $\bar{\zeta}$ . Prior to SEF during flight A1 (Fig. 3), maximum  $\bar{\zeta}$  ( $24 \times 10^{-4} \text{ s}^{-1}$ ) was located at the 20-km radius, inward of the primary  $\bar{v}_{\text{max}}$ , and sharply declined from this maximum out to 55 km. From  $r = 55\text{--}100 \text{ km}$ ,  $\bar{\zeta}$  gradually decreased, which was indicative of a beta skirt and consistent with the vorticity structures seen in other mature hurricanes (Mallen et al. 2005). During SEF in flight A2,  $\bar{\zeta}$  noticeably increased to approximately  $7 \times 10^{-4} \text{ s}^{-1}$  from  $r = 75\text{--}90 \text{ km}$ , corresponding to a strengthening secondary  $\bar{v}_{\text{max}}$ . The increased  $\bar{\zeta}$  in the beta-skirt region during flight A2 was similarly displayed in Terwey and Montgomery's (2008) simulations. The decreased inner  $\bar{\zeta}$  maximum ( $15 \times 10^{-4} \text{ s}^{-1}$ ) reflects the weakened inner  $\bar{v}_{\text{max}}$ . By flight A3,  $\bar{\zeta}$  exhibited a broad decrease with radius, consistent with a broader circulation post-ERC. Overall, the structure of  $\bar{\zeta}$  fundamentally changed during Bonnie's ERC.

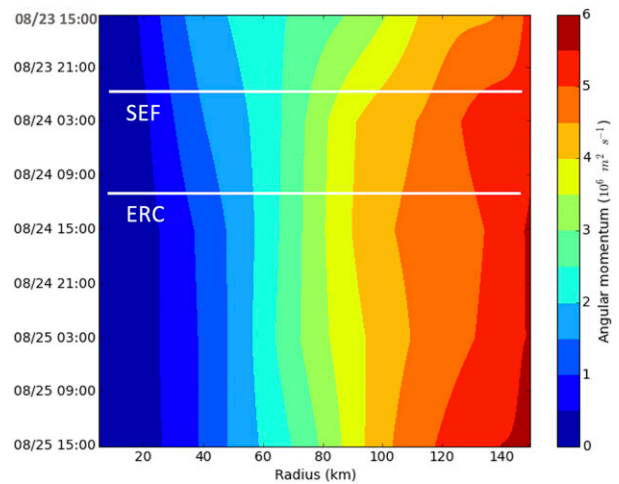


FIG. 4. Radius vs time Hovmöller of flight-level (700 hPa) absolute angular momentum ( $10^6 \text{ m}^2 \text{ s}^{-1}$ ) from 1500 UTC 23 Aug to 1500 UTC 25 Aug. White lines labeled SEF and ERC denote the times during which Bonnie's secondary eyewall formation and eyewall replacement cycle occurred at 0000 UTC 24 Aug and 1200 UTC 24 Aug, respectively.

Figures 2 and 3 show a very weak  $\bar{v}_{\text{max}}$  and  $\bar{\zeta}_{\text{max}}$  near the 120-km radius during flight A1. Kepert (2013, 2017) argued that even a weak  $\bar{\zeta}_{\text{max}}$  can organize into an outer eyewall through a feedback between boundary layer frictional convergence and convection. It is possible that the outer  $\bar{v}_{\text{max}}$  shifted inward from 120 to 85 km between 1200 UTC 23 August and 0000 UTC 24 August. If so, Bonnie's speed of contraction was approximately  $1 \text{ m s}^{-1}$ , which is consistent with the typical speed of contraction for outer eyewalls of  $0.5\text{--}1 \text{ m s}^{-1}$  (S11).

The possible role of the  $\bar{v}_{\text{max}}$  is addressed in Hovmöller diagrams in Figs. 4 and 5. The development of the secondary  $\bar{v}_{\text{max}}$  can be seen in  $\bar{m}_a$  and radial wind ( $\bar{u}$ ) contours, and in Fig. 5b. Prior to and during SEF,  $\bar{m}_a$  contours bowed inward from 80 to 150 km, while contours shifted slightly outward in the core ( $<60 \text{ km}$  in radius). The reason for this evolution is seen in  $\bar{u}$  (Fig. 5a): late on 23 August and early on 24 August, almost continuous outflow from inner radii reaches to about the 80-km radius. Simultaneously, strong inflow outside that radius implies convergence here and carries in large  $\bar{m}_a$  directly where  $\bar{v}$  dramatically increased in the secondary eyewall. The rapid spinup of the outer  $\bar{v}_{\text{max}}$  (Fig. 5b) during this time is consistent with this implied strong convergence field. It is notable that the very weak  $\bar{v}_{\text{max}}$  at the 120-km radius does not even show in the Hovmöller diagram of  $\bar{v}$ . This suggests the very weak  $\bar{v}_{\text{max}}$  did not contract, but instead an in situ development within the beta skirt led to the secondary eyewall.

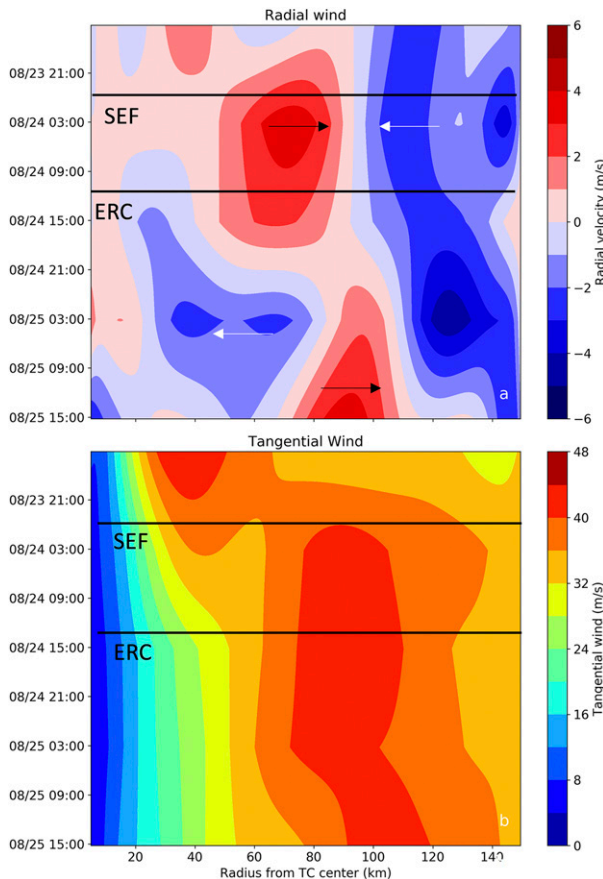


FIG. 5. As in Fig. 4, but for (a) radial velocity ( $\text{m s}^{-1}$ ) and (b) tangential velocity ( $\text{m s}^{-1}$ ). In (a) arrows indicate the direction of radial velocity at certain times, where blue (red) is inflow (outflow).

### b. Comparison with ERC climatology

Bonnie had substantial departures compared to variables from Kossin and Sitkowski's (2009) ERC predictor model for ERCs in 45 North Atlantic TCs (Table 2). In particular, variables related to shear (200-hPa zonal wind, 850–200-hPa shear magnitude, and standard deviation of GOES infrared brightness temperature) clearly differ. The 200-hPa zonal wind was  $8.7 \text{ m s}^{-1}$  (17 kt) in Bonnie and only  $5.7 \text{ m s}^{-1}$  (11 kt) for TCs with ERCs, shear magnitude was  $14.9 \text{ m s}^{-1}$  (29 kt) in Bonnie and  $5.7 \text{ m s}^{-1}$  (11 kt) in other ERCs, and standard deviation of GOES infrared brightness temperature was  $16.7^\circ\text{C}$  in Bonnie and  $12.6^\circ\text{C}$  in other TCs. The 0–600-km average symmetric tangential wind was also stronger in Bonnie at  $17.3 \text{ m s}^{-1}$ , whereas it was  $10.9 \text{ m s}^{-1}$  in other TCs with ERCs, suggestive of Bonnie's broader vortex.

Bonnie's anomalous values at 0000 UTC 24 August are apparent when comparing them with probability density functions (PDFs; Fig. 6) of these variables for TCs with and without ERCs. For both 200-hPa zonal wind (Fig. 6a) and

shear magnitude (Fig. 6b), Bonnie falls outside the highest range usually encountered in TCs with ERCs. Bonnie's standard deviation of GOES infrared brightness temperature (Fig. 6c) and 0–600-km average symmetric tangential wind (Fig. 6d) are on the upper end of the distribution. While higher values of 200-hPa zonal wind and 0–600-km average symmetric tangential wind in Bonnie are consistent with the occurrence of an ERC, the anomalous nature of these values make the characteristics of Bonnie's ERC unique. Thus, Bonnie experienced higher shear, was more asymmetric, and was broader compared to other ERC events.

### c. Asymmetric evolution

To visualize Bonnie's asymmetric evolution, SSM/I 85-GHz microwave images were examined (Fig. 7). As discussed by Cecil et al. (2002), brightness temperatures  $<215 \text{ K}$  at the 85-GHz frequency suggest convection, while brightness temperatures  $>215 \text{ K}$  imply stratiform precipitation. Bonnie exhibited a highly asymmetric structure at 1335 UTC 23 August (Fig. 7a) when shear was  $12 \text{ m s}^{-1}$  from the northwest. Both inner core convection ( $<215 \text{ K}$ ; red and white) and outer stratiform precipitation ( $>215 \text{ K}$ ; yellow and green) were located almost exclusively downshear, as might be expected in strong shear. By 0053 UTC 24 August (Fig. 7b), precipitation extended from downshear to upshear from  $r = 100$  to  $150 \text{ km}$ . This quasi-circular band (brightness temperatures  $<240 \text{ K}$ ) was the nascent secondary eyewall forming and overtaking the primary eyewall, which was located downshear at  $r = 30$ – $50 \text{ km}$ . Just under 13 h later (Fig. 7c), the secondary eyewall (now the only eyewall) intensified and extended farther upshear. At this time, the primary eyewall was no longer evident, indicating the conclusion of Bonnie's ERC.

LF radar images (Fig. 8) focus on a 4-h period prior to the time of Fig. 7b, when the outer wind maximum first appeared in the symmetric wind (Fig. 2). From 1212 UTC 23 August to 0021 UTC 24 August (Figs. 8a–f), an intense and highly asymmetric primary eyewall was located downshear-left at approximately  $35 \text{ km}$ . A strong shear signature is seen by the lack of convection upshear in the core. Surrounding the primary eyewall at 1212 UTC was a rainband that wrapped around from downshear right to upshear left from  $80$  to  $120 \text{ km}$  (Fig. 8a). This rainband intensified and organized from 2115 (Fig. 8c) to 2350 UTC 23 August (Fig. 8e), growing in size with  $>30 \text{ dBZ}$  reflectivity from  $75$  to  $150 \text{ km}$ . The most intense rainband region to the north-northeast (left of shear) was centered at the  $100 \text{ km}$  radius at 2350 UTC 23 August. By 0021 UTC 24 August (Fig. 8f), the rainband transitioned to a secondary eyewall, as evidenced by the three-quarters of a ring of high reflectivity extending from downshear right to upshear left from  $80$  to  $110 \text{ km}$ .

TABLE 2. SHIPS features used in Kossin and Sitkowski's (2009) Eyewall Replacement Cycle Predictor (pERC) model. The mean values for hurricanes undergoing (secondary eyewall formation imminent in the next 12 h) and not undergoing an eyewall replacement cycle (ERC; indicated by "ERC yes" and "ERC no", respectively). The values for these features in Bonnie at the time of secondary eyewall formation (0000 UTC 24 Aug) are also shown for comparison. (Data provided by J. Kossin.)

SHIPS feature	ERC yes (mean)	ERC no (mean)	Bonnie (0000 UTC 24 Aug)
Current intensity	110.41 kt	86.17 kt	100 kt
Latitude	21.67°	27.04°	24.80°
Climatological depth of 26°C isotherm	95.43 m	66.48 m	54 m
200-hPa zonal wind (200–800 km from center)	11.04 kt	8.62 kt	16.9 kt
500–300-hPa relative humidity	50.21%	45.14%	49%
0–600-km average symmetric tangential wind at 850 hPa from NCEP analysis	10.88 m s <sup>-1</sup>	8.84 m s <sup>-1</sup>	17.3 m s <sup>-1</sup>
Azimuthally averaged surface pressure at outer edge of vortex	1013.9 hPa	1015.5 hPa	1012 hPa
850–200-hPa shear magnitude	11.13 kt	18.15 kt	29.1 kt
Max potential intensity	136.35 kt	118.73 kt	145 kt
Std dev (from axisymmetry) of GOES IR brightness temperature between 100 and 300 km	12.59°C	16.61°C	16.7°C
Avg GOES IR brightness temperature between 20 and 120 km	-63.09°C	-54.74°C	-68.8°C

This upshear extension of the secondary eyewall raises the question: Why did shear not inhibit SEF in the traditionally unfavorable upshear region? To address this question, downshear and upshear dropsonde composites of wind speed in the SEF region ( $r = 70$ – $100$  km) during SEF (2000 UTC 23 August–0020 UTC 24 August) and during the entire observation period (1200 UTC 23 August–0000 UTC 25 August) were examined (Fig. 9). Near-surface wind speeds provided a proxy for surface fluxes, which is important in understanding convective development. A sharply higher surface wind speed occurred upshear ( $38 \text{ m s}^{-1}$ ) during SEF (Fig. 9a), which was nearly 35% higher than downshear ( $25 \text{ m s}^{-1}$ ). Even after SEF concluded (Fig. 9b), higher surface wind speeds upshear continued and were over a deeper layer (up to 800 hPa) compared to during SEF. Stepped Frequency Microwave Radiometer (SFMR) data support the upshear surface wind speed maxima in the SEF region, but with a smaller difference of 10%–15% in upshear–downshear wind speeds. The reason for the discrepancy is not certain, but it is notable that both methods support the maximum surface winds upshear. An upshear surface wind speed maximum was similarly observed in Klotz and Jiang (2017) when the storm motion and the shear vectors opposed one another, as was the case in Hurricane Bonnie.

#### d. Concentric eyewall structure–3D Doppler analyses

Three-dimensional Doppler analyses from the TA radar centered at approximately 0000 UTC 24 August provide further insight into the double-eyewall structure. Broad wind speed maxima over  $45 \text{ m s}^{-1}$  were located on the eastern and northern side of Bonnie at 2 km in altitude (Fig. 10a), consistent with the location

of primary and secondary eyewall reflectivity maxima (Fig. 8). Above 2 km, wind speed maxima were more discrete (Figs. 10b–d), but still predominantly seen on the eastern and northern side of Bonnie. While the distribution of scatterers is insufficient to quantitatively calculate a tilt using a simplex-like algorithm (e.g., Reasor et al. 2009), a qualitative assessment can be made by examining the location of the minimum wind speed and Earth-relative circulation center. The minimum wind speed in Fig. 10 (bottom of color bar) lies near  $r = 0$  at  $z = 2$  and 5 km. At  $z = 8$  and 11 km, the minimum wind speed lies about 25 km to the south-east. This displacement of minimum wind speed is suggestive of a downshear tilt of the inner vortex.

North–south cross sections (Fig. 11) display the double eyewall vertical structure, in which shear-forced asymmetries are apparent. To the north (left of shear), the inner eyewall is seen by a narrow 15–25-dBZ reflectivity tower at approximately 30 km in radius extending up to 15 km (Fig. 11a). A broader area of 20–35-dBZ reflectivity from 70 to 125 km in radius characterized the secondary eyewall. To the south (right of shear), reflectivity was more suppressed, especially in the primary eyewall region, where a coherent structure was lacking. However, a reflectivity maximum was located in the secondary eyewall region, at approximately 85–100 km to the south. Collocated with these double eyewall reflectivity maxima were double wind maxima (Fig. 11a), most distinct around 3 km in height. These wind maxima ranged in magnitude from  $40$  to  $50 \text{ m s}^{-1}$  ( $40$ – $45 \text{ m s}^{-1}$ ) to the north (south). The northern secondary eyewall, which exhibited the strongest convection, also contained the deepest  $45 \text{ m s}^{-1}$  wind (up to 4 km in height).

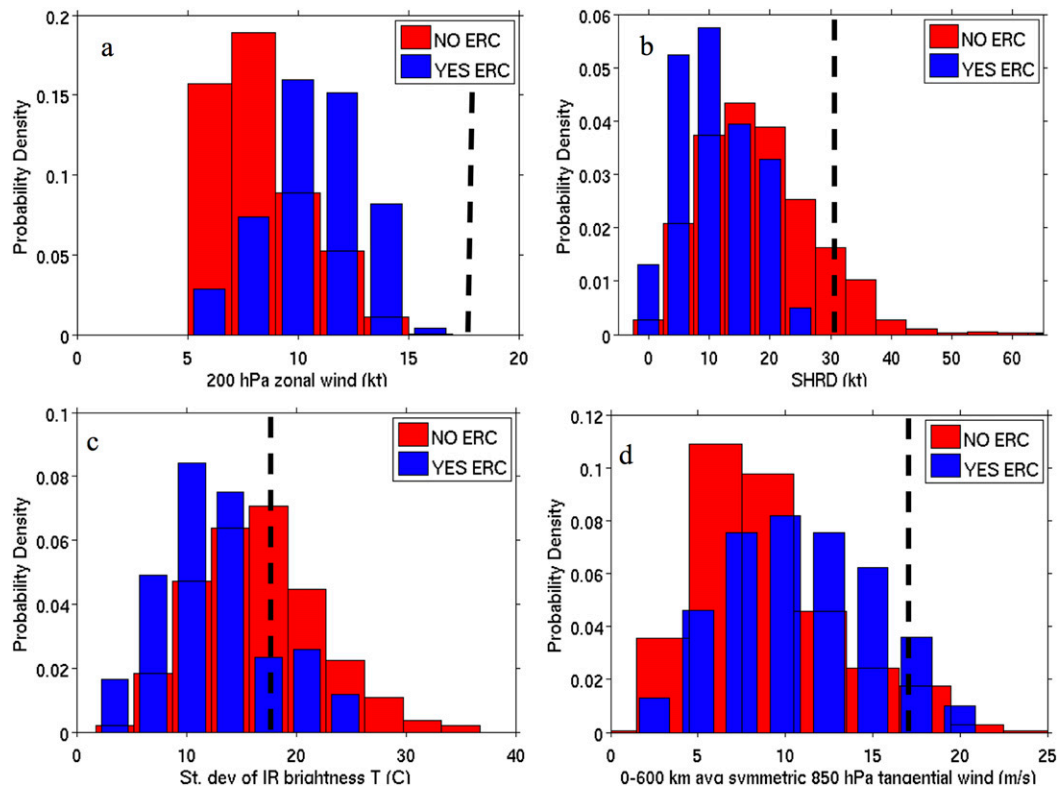


FIG. 6. Probability density function (PDF) of (a) 200-hPa zonal wind (kt;  $1 \text{ kt} \approx 0.5144 \text{ m s}^{-1}$ ), (b) shear magnitude (SHRD; kt), (c) standard deviation of infrared brightness temperature ( $^{\circ}\text{C}$ ), and (d) 0–600-km average symmetric tangential wind ( $\text{m s}^{-1}$ ) for TCs undergoing (“YES ERC”) and not undergoing an ERC (“NO ERC”) from Kossin and Sitkowski’s (2009) database of 45 North Atlantic hurricanes. The dashed black line indicates Bonnie’s value at the time of its secondary eyewall formation at 0000 UTC 24 Aug. (Data and plotting routine for PDFs courtesy of Dr. James Kossin.)

A vertical velocity cross section (Fig. 11b) displays an asymmetric signature, particularly at the radius of the primary eyewall, which is consistent with the greater than wavenumber-0 asymmetry in ice scattering seen in the microwave (Fig. 7) and reflectivity from the radar data (Fig. 8). Left of shear was characterized predominantly by downward motion, while right of shear contained mostly upward motion. Downdrafts were strongest at approximately 25–30 km in radius throughout most of the troposphere to the north, where values ranged from 2 to  $5 \text{ m s}^{-1}$ . Didlake et al. (2017) similarly observed strong downdrafts in Hurricane Gonzalo’s (2014) decaying primary eyewall. Updrafts maximized at 45–50 km in radius to the south throughout much of the troposphere, reaching magnitudes of  $2\text{--}5 \text{ m s}^{-1}$ . In the vicinity of the secondary eyewall ( $\sim 75 \text{ km}$ ), both the north and south sides contained upward motion. However, to the south, these updrafts covered a broader region from approximately 60–110 km and only were  $1\text{--}2 \text{ m s}^{-1}$  at their maximum. To the north, a band of  $0.2\text{--}5 \text{ m s}^{-1}$  updrafts started at the surface 75 km in radius and ascended in height radially outward to approximately 125 km in radius. Directly

beneath this band of updrafts from 5 to 8 km in height were  $0.5\text{--}2 \text{ m s}^{-1}$  downdrafts from 85 to 100 km in radius.

The vertical vorticity cross section (Fig. 11c) is consistent with a possible wavenumber-1 asymmetry suggested by the asymmetries in the microwave and radar data (cf. Figs. 7 and 8). To the south, where there was predominantly rising motion, vorticity appeared enhanced compared to the north, particularly at 20 km in radius. Vorticity was generally maximized within 50 km both north and south near the primary eyewall, consistent with observations of mature hurricanes (Mallen et al. 2005). A low-level positive vorticity maximum existed outside of the primary eyewall, at 75 km in radius to the north. This positive vorticity band was nearly collocated with the ascending updrafts, wind speed maximum, and reflectivity maximum that characterized the secondary eyewall.

## 5. Discussion

### a. Comparison with other ERCs

Hurricane Bonnie’s evolution was atypical in numerous regards: rapid intensification occurred as shear

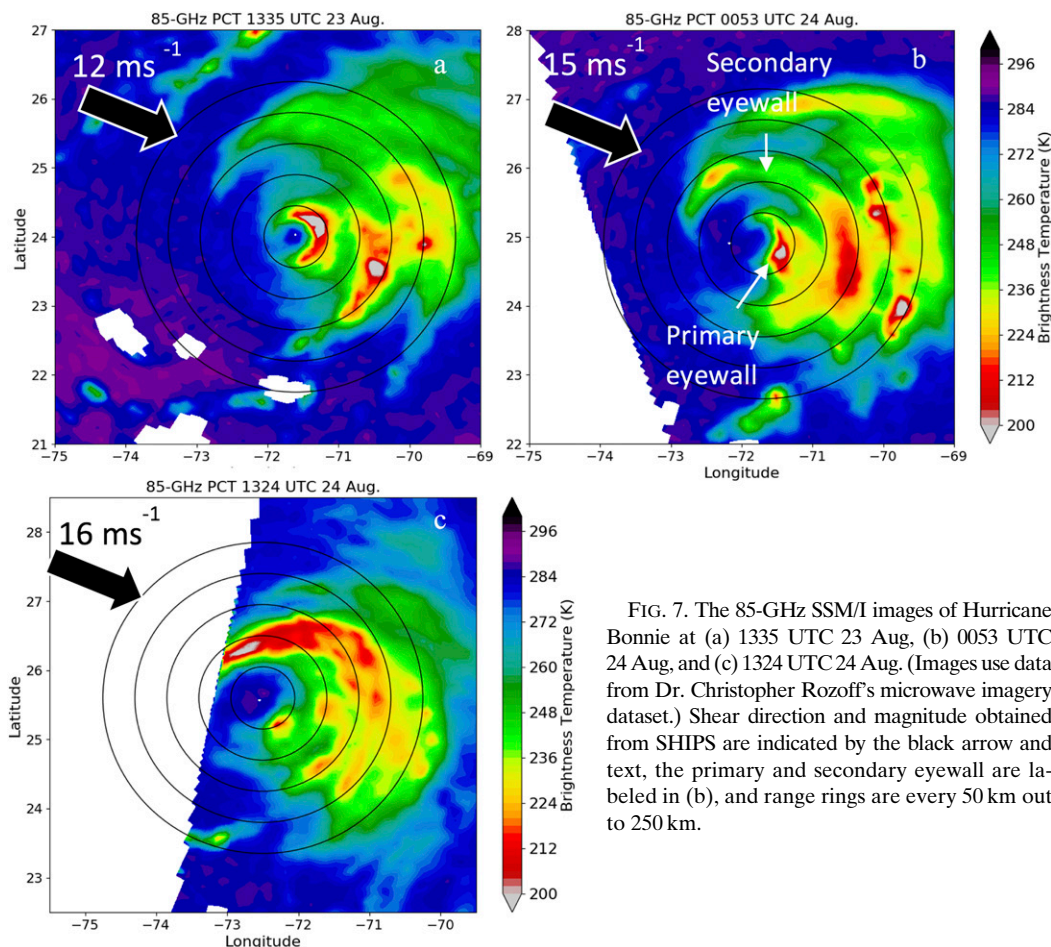


FIG. 7. The 85-GHz SSM/I images of Hurricane Bonnie at (a) 1335 UTC 23 Aug, (b) 0053 UTC 24 Aug, and (c) 1324 UTC 24 Aug. (Images use data from Dr. Christopher Rozoff's microwave imagery dataset.) Shear direction and magnitude obtained from SHIPS are indicated by the black arrow and text, the primary and secondary eyewall are labeled in (b), and range rings are every 50 km out to 250 km.

increased and rainbands supported by warm SSTs developed into a secondary eyewall with an upshear surface wind maximum (due to oppositely pointing shear and motion vectors; Klotz and Jiang 2017). These ingredients combined to allow SEF to occur under strong shear. The strong shear-induced asymmetries observed in Hurricane Bonnie differ from the typical view of an ERC being largely symmetric. These differences are highlighted by Bonnie's stronger 200-hPa zonal wind, larger 850–200-hPa shear magnitude, greater standard deviation of GOES brightness temperature, and stronger 0–600-km average symmetric tangential wind (Table 2 and Fig. 6) compared to other ERCs. Though stronger 200-hPa zonal wind and 0–600-km average symmetric tangential wind is consistent with observed ERCs, Bonnie's anomalously large values compared to other ERCs makes Bonnie's ERC unique. Thus, Bonnie was anomalously broad, more asymmetric, and encountered higher shear during its ERC than other storms. Also unlike other ERCs, Bonnie did not change intensity, nor did the secondary eyewall appear to contract (Fig. 2).

Despite its anomalies, Hurricane Bonnie still exhibited some similarities to "classic" ERCs. An asymmetric secondary  $v_{\max}$  was first detected downshear during flight A1 (not shown) pre-SEF, as in S11 (recall that during and after SEF, a wind maximum was observed upshear). By flight A2, this asymmetric  $v_{\max}$  projected onto the azimuthal mean (i.e., secondary  $\bar{v}_{\max}$ ; Fig. 2). The subsequent development, strengthening, and dominance of the secondary  $\bar{v}_{\max}$  that occurred while the primary  $\bar{v}_{\max}$  decayed in Bonnie (Fig. 2) are consistent with the progression of wind maxima described by S11 and Willoughby et al. (1982). Additionally, the changes in the overall radial  $\bar{\zeta}$  structure during SEF, particularly the development of the secondary  $\bar{\zeta}$  maximum, were similarly observed by Abarca and Corbosiero (2011) in Hurricanes Katrina and Rita.

#### b. Evolution of Bonnie's ERC

##### 1) PRE-SEF (0000–1200 UTC 23 AUGUST; FIG. 7A)

Early on 23 August, Bonnie rapidly intensified to a major hurricane status (Fig. 1), despite an increase in

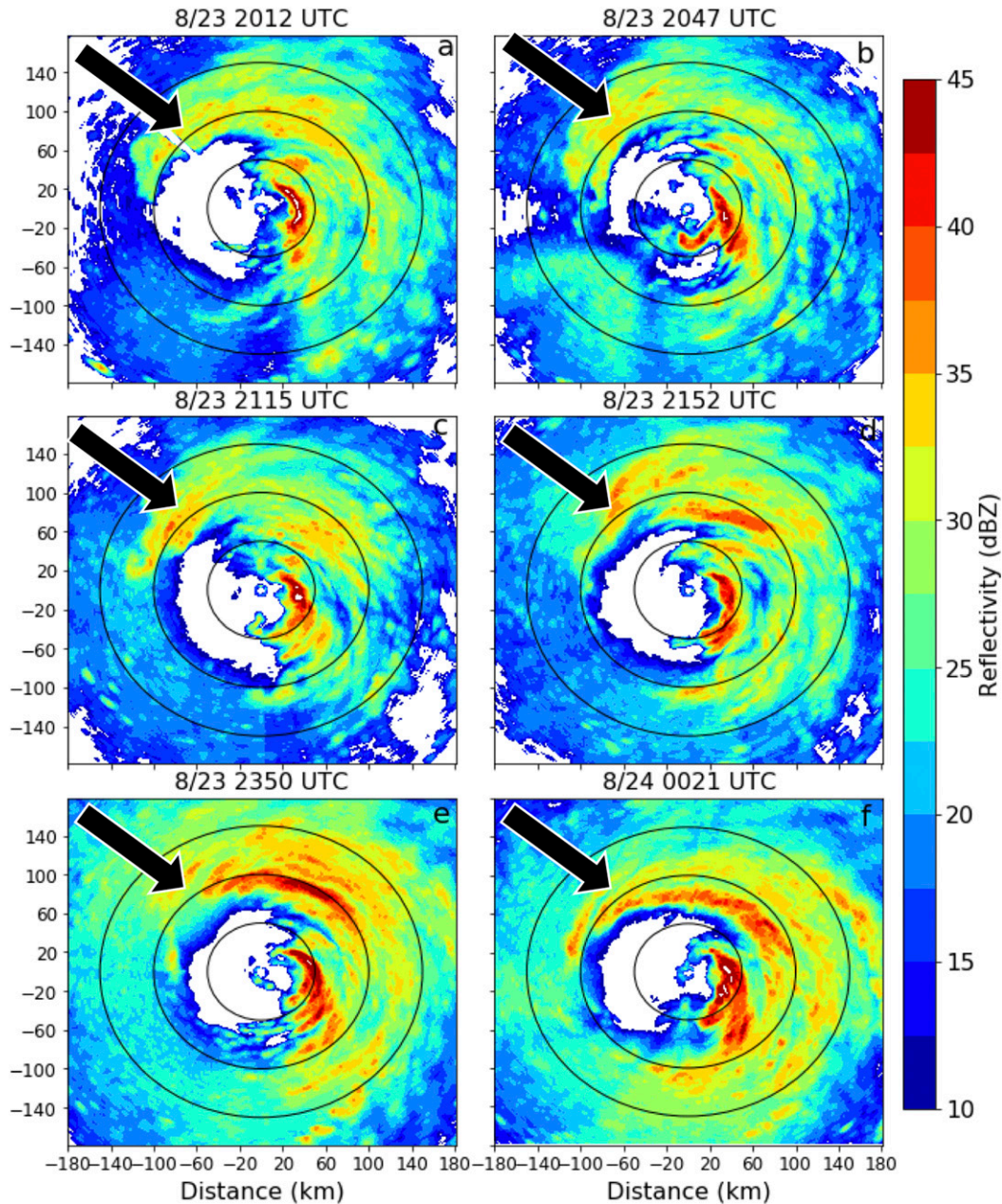


FIG. 8. Lower fuselage radar reflectivity images during Bonnie's secondary eyewall formation at (a) 2012 UTC 23 Aug, (b) 2047 UTC 23 Aug, (c) 2115 UTC 23 Aug, (d) 2152 UTC 23 Aug, (e) 2350 UTC 23 Aug, and (f) 0021 UTC 24 Aug. Range rings are every 50 km and shear direction is denoted by the black arrow.

vertical wind shear from  $2$  to  $12 \text{ m s}^{-1}$ . High SSTs (over  $28^\circ\text{C}$ ) were likely encountered by Bonnie (Heymisfield et al. 2001), prior to a slowed storm movement and an upwelling of cooler SSTs later on 23 August and 24 August (Wentz et al. 2000). These high SSTs and persistently stronger shear forcing might have created a conducive environment for the initial development of downshear rainbands well outside the

primary eyewall, from  $r = 100$  to  $250$  km at 1200 UTC 23 August (Fig. 7a). The primary eyewall was highly asymmetric, with convection downshear and downshear left. No axisymmetric wind maximum was present at larger radii, but a local wind maximum occurred downshear. A broadened circulation was observed by the decrease in Mallen et al.'s (2005)  $\alpha$  parameter from 0.35 early on 23 August to 0.26 at 1200 UTC

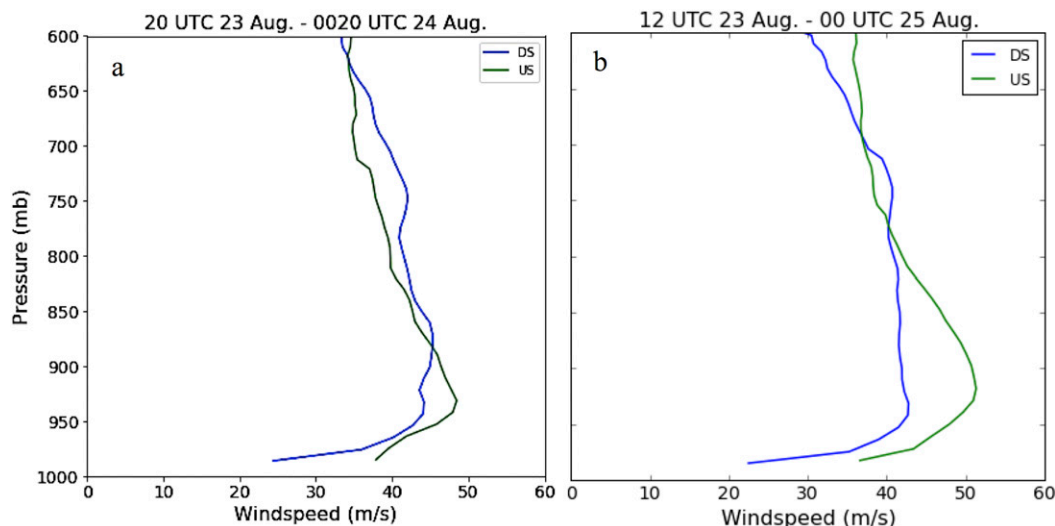


FIG. 9. Shear-relative (DS = downshear, US = upshear) dropsonde composites of wind speed in the secondary eyewall region (70–100 km), during (a) 2000 UTC 23 Aug–0020 UTC 24 Aug and (b) 1200 UTC 23 Aug–0000 UTC 25 Aug. DS (US) composites include (a) 5 (7) dropsondes and (b) 8 (14) dropsondes from NOAA P-3 flights.

23 August. At this point, Bonnie was a major hurricane, yet it was substantially broader than the average  $\alpha = 0.48$  for a major hurricane (Mallen et al. 2005). This broadened circulation is hypothesized to be driven by the extensive downshear convection outside the storm core. It is likely that strong shear created a favorable environment outside of the primary eyewall for enhanced upward motion, winds, and convection downshear (Frank and Ritchie 2001; Corbosiero and Molinari 2002).

## 2) SEF (1200 UTC 23 AUGUST–0000 UTC 24 AUGUST; FIG. 7B)

Vertical wind shear continued to increase, up to  $15 \text{ m s}^{-1}$ , as Bonnie maintained a steady  $51 \text{ m s}^{-1}$  intensity. More extensive convection developed at outer radii (100–250 km; Figs. 7b and 8), and extended into the upshear quadrants. SEF was indicated at 0000 UTC 24 August by this nearly concentric band of precipitation (Figs. 7b and 8f) and the stronger secondary wind maximum (Fig. 2). The upshear extension of the secondary eyewall was associated with stronger surface wind speeds upshear (Fig. 9a). Although upshear wind maxima are rare (e.g., Uhlhorn et al. 2014), Klotz and Jiang (2017) found such a distribution when the storm motion and the shear vectors opposed one another, as was the case in Hurricane Bonnie. Though the cause of the upshear surface wind maxima is uncertain, it defined the upshear extension of the outer eyewall and likely supported enhanced surface fluxes and convection.

The primary eyewall remained highly asymmetric during this time, more so than the secondary eyewall, which suggests a greater susceptibility to shear. This result was

similar to Didlake et al.'s (2017) observations in Hurricane Gonzalo (2014) and might be explained by potential vorticity arguments. Upshear subsidence is driven by negative potential vorticity advection by cross-storm flow (DeMaria 1996; Bender 1997), and for a given cross-storm flow, advection is greatest at the largest potential vorticity radial gradient. Initially, during Bonnie's SEF, the largest potential vorticity radial gradient likely existed in the primary eyewall, which resulted in greater subsidence.

Furthermore, the azimuthal phase of the reflectivity maxima differed between the primary and secondary eyewall. The left-of-shear reflectivity maximum in the secondary eyewall (Figs. 8 and 11) was shifted downwind of the downshear primary eyewall reflectivity maximum (Fig. 8). Didlake et al. (2017) similarly noted a downwind shift in Hurricane Gonzalo's (2014) concentric eyewalls' reflectivity maxima. They speculated that the primary eyewall's asymmetry was forced by a shear-induced tilt, while the secondary eyewall's asymmetry was due to an interaction with a rainband complex.

## 3) ERC (0000 UTC 24 AUGUST–1200 UTC 24 AUGUST; FIG. 7C)

Bonnie's ERC completed at 1200 UTC 24 August, indicated by the appearance of only a single axisymmetric tangential wind maximum at  $r = 85 \text{ km}$  (Fig. 2). The primary eyewall collapsed (Fig. 7c), while convection in the secondary (now only) eyewall intensified from left of shear to upshear. Surface wind speeds remained larger upshear than downshear in this outer eyewall (Fig. 9b). However, it remains unclear whether enhanced surface fluxes (due to higher surface wind speeds) excited

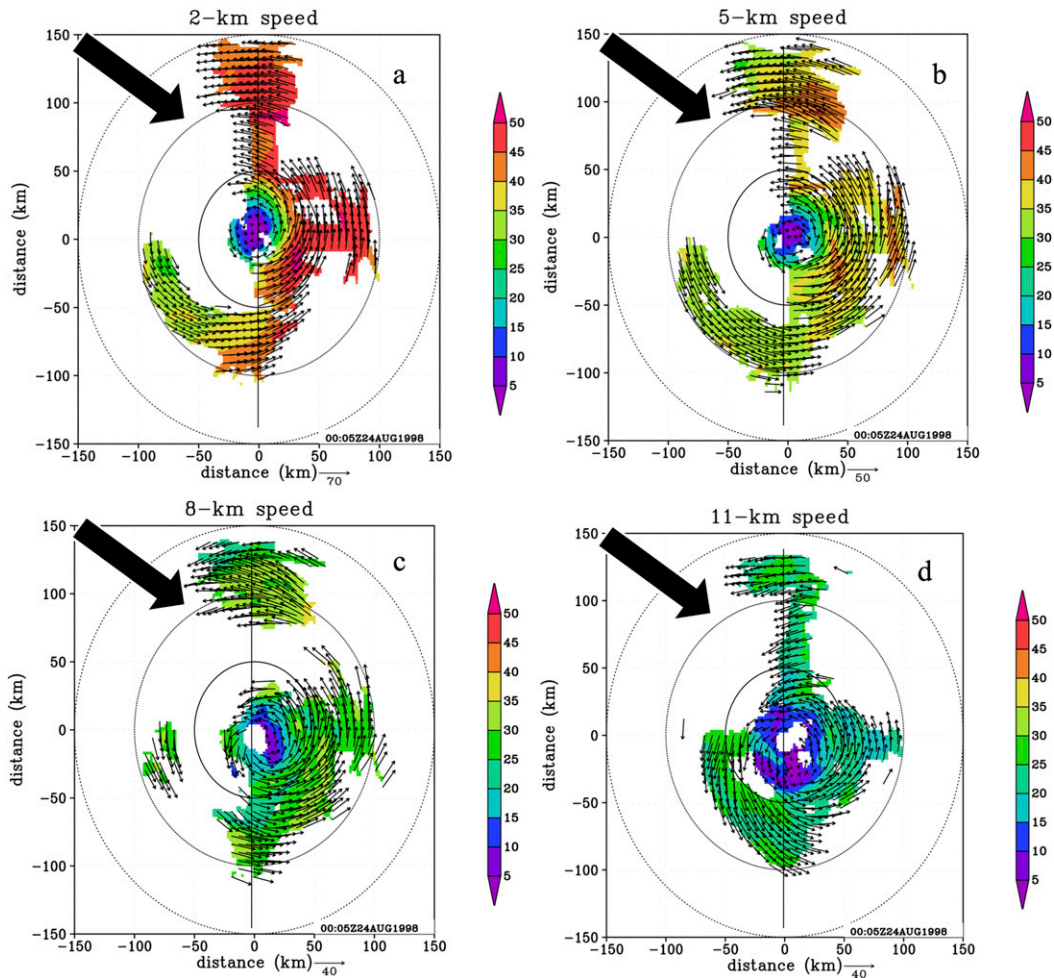


FIG. 10. Tail Doppler wind speed (color) and direction (arrows) at (a) 2, (b) 5, (c) 8, and (d) 11 km as a function of distance from Bonnie’s center. The black solid, dashed, and dot–dashed rings indicate the 50-, 100-, and 150-km radius, respectively. Wind speed analyses are centered at approximately 0000 UTC 24 Aug. Black north–south vertical lines denote the cross-sectional location used in Fig. 11, while black arrows denote the shear vector.

enhanced convection upshear, or enhanced left-of-shear convection produced downwind wind speed maxima. Regardless of the sequence of events, it is hypothesized that enhanced surface fluxes upshear played an important role in Bonnie’s SEF by aiding the increase of convectively generated  $\zeta$  at outer radii (Fig. 11c). These enhanced surface fluxes upshear were due to stronger upshear surface winds (Fig. 9), which was the result of oppositely pointing shear and motion vectors (Klotz and Jiang 2017). It is possible that this unusual configuration of shear and motion vectors allowed for Bonnie’s ERC to occur under the influence of strong shear.

*c. Bonnie’s SEF*

Other SEF theories might have been factors in Bonnie’s SEF. The beta-skirt region has been known to be favorable for SEF, as it is conducive to the generation

and outward propagation of vortex Rossby waves (Corbosiero et al. 2006; Abarca and Corbosiero 2011) and can transfer convectively generated vorticity perturbations into the azimuthal mean flow (Terwey and Montgomery 2008). Bonnie displayed a beta skirt in its radial  $\bar{\zeta}$  structure during flight A1 from 55 to 100 km (Fig. 3). The secondary  $\bar{v}_{max}$  developed at 85 km (Fig. 2). The appearance of the secondary  $\bar{v}_{max}$  close to 3 times the primary  $\bar{v}_{max}$  (cf. wind speed curves in Fig. 2) might indicate the presence of vortex Rossby waves (Montgomery and Kallenbach 1997; Corbosiero et al. 2006; Terwey and Montgomery 2008). With limited observational data, the presence of vortex Rossby waves cannot be determined.

Regardless of the mechanism, the increased  $\bar{\zeta}$  associated with SEF that occurred near the outer edge of the beta skirt is consistent with Terwey and Montgomery (2008).

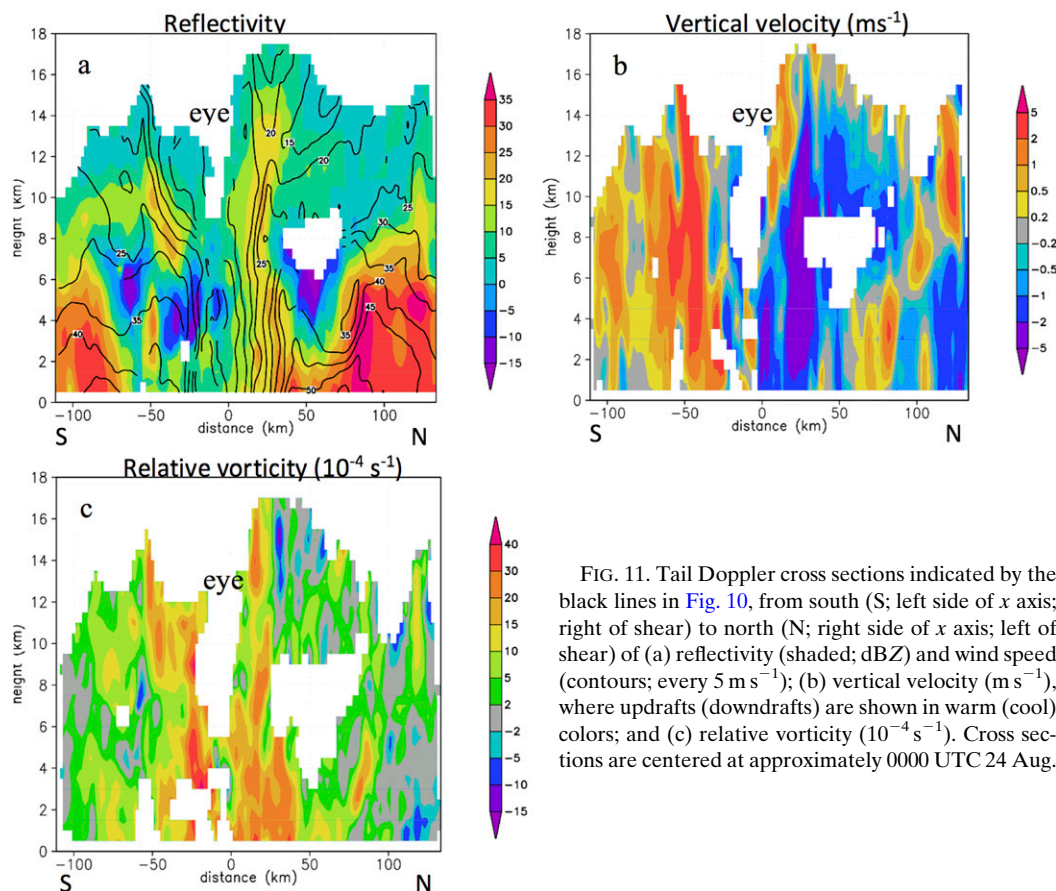


FIG. 11. Tail Doppler cross sections indicated by the black lines in Fig. 10, from south (S; left side of  $x$  axis; right of shear) to north (N; right side of  $x$  axis; left of shear) of (a) reflectivity (shaded; dBZ) and wind speed (contours; every  $5 \text{ m s}^{-1}$ ); (b) vertical velocity ( $\text{m s}^{-1}$ ), where updrafts (downdrafts) are shown in warm (cool) colors; and (c) relative vorticity ( $10^{-4} \text{ s}^{-1}$ ). Cross sections are centered at approximately 0000 UTC 24 Aug.

However, Terwey and Montgomery (2008) focused on a low-level ( $<2 \text{ km}$ ) beta skirt, whereas the beta skirt in the present study could only be detected at 700 hPa because of continuous observations below, so it is assumed that this 700-hPa beta skirt in Bonnie extended to lower levels. A source of convection in the beta-skirt region is needed following Terwey and Montgomery's (2008) hypothesis, which might have been provided by shear-induced tilt. Microwave imagery (Fig. 7a) prior to SEF (1335 UTC 23 August) exhibited downshear convection at approximately 100 km, which is just beyond the beta skirt, and thus not entirely consistent with Terwey and Montgomery's (2008) hypothesis. It is possible that sporadic convection developed within the beta skirt prior to SEF but was not captured on the resolution of the microwave imagery, though this is uncertain.

The unbalanced boundary layer spinup mechanism of SEF (Huang et al. 2012; Abarca and Montgomery 2013, 2015; Abarca et al. 2016) is another possible contribution to Bonnie's SEF. Through this framework, it is suggested that SEF occurs via the following sequence of events: a broadening of the tangential wind field, increased boundary layer inflow, boundary layer convergence caused by the supergradient flow that decelerates inflow,

and compensating upward motion that supports convection in a favorable thermodynamic environment to promote secondary eyewall development (Huang et al. 2012). Though a broadening of the tangential winds (above the boundary layer; Fig. 2) and strong boundary layer inflow (outside Bonnie's secondary eyewall region, the dropsonde spatial and temporal resolution was not fine enough to calculate the gradient force in the boundary layer like in Abarca et al. (2016). Thus, while unbalanced boundary layer processes possibly contributed to Bonnie's SEF, it is beyond the scope of the current study to demonstrate.

It has furthermore been suggested that the strength of rainband convection relative to the inner eyewall is a potential determinant of SEF. Rozoff et al. (2012) and Zhu and Zhu (2014) hypothesized that rainband convection must be of sufficient strength in order for rainbands to develop into a secondary eyewall via axisymmetrization of rainband heating and feedback processes between convection, convergence, radial inflow, tangential wind acceleration, and moist instability, respectively. While it is observed that SEF ensues in Bonnie once convection at outer radii became stronger than the primary eyewall convection (Fig. 7b) at approximately

0000 UTC 24 August, this is attributed to the aid of upshear-enhanced surface fluxes in increasing convectively generating  $\zeta$  to support secondary eyewall convection [section 5b(3)] rather than axisymmetrization alone.

#### d. Intensity change

During Bonnie's steady-state phase from 24 to 26 August, airborne XBT (AXBT) measurements observed significantly cooler SSTs (average of 27°C) in Bonnie. This cooling is consistent with the shallow oceanic mixed layer under Bonnie (Table 2) and is in contrast to the warm SSTs in Bonnie through 1200 UTC 23 August (Heymsfield et al. 2001; Molinari and Vollaro 2008). The AXBT results confirm Wentz et al.'s (2000) findings of cooler SSTs (25°–27°C) observed from 24 to 26 August by the Tropical Rainfall Measuring Mission (TRMM) Microwave Imager (TMI). However, since Wentz et al.'s (2000) observations covered a 2-day period, the effect of SST changes on Bonnie's resiliency cannot be conclusively determined. It seems likely that warm SSTs preceded Bonnie's passage from 24 to 26 August, after which SSTs cooled as Bonnie's storm movement slowed (not shown). It is thus believed that SSTs did not have a major influence on Bonnie's resiliency during the period from 24 to 26 August.

It is instead speculated that Bonnie's larger radius of maximum winds during and post-ERC contributed to Bonnie's resiliency in high shear. The expansion of the radius of maximum winds from 35 to 85 km between 1400 UTC 23 August and 1400 UTC 24 August could support Jones's (1995) and DeMaria's (1996) findings that larger storms are more resistant to shear. Additionally, an increased radius of maximum wind means diabatic heating within the radius of maximum winds was more likely, which would increase the efficiency of intensification (Nolan et al. 2007; Pendergrass and Willoughby 2009; Vigh and Schubert 2009). Diabatic heating within Bonnie's larger radius of maximum winds was seen by the intense primary eyewall situated inside the secondary eyewall at 0000 UTC 24 August (Fig. 8f).

Hurricane Bonnie was an exceptional case of a highly resilient hurricane that underwent an ERC while embedded in strong shear. Vertical wind shear usually inhibits TC intensification, but significant exceptions occur in which highly sheared storms rapidly intensify (Shelton and Molinari 2009; Molinari and Vollaro 2010; Nguyen and Molinari 2012). Analogously, ERCs usually develop in low-shear, fairly symmetric storms. The case of Hurricane Bonnie (and that of Didlake et al. 2017) suggests that it might be fruitful to examine eyewall replacement cycles during periods of moderate and strong vertical wind shear.

*Acknowledgments.* We thank HRD scientist, Nancy Griffin, for obtaining 1998 radar data and Dr. Frank Marks, Dr. Paul Reasor, and Dr. John Gamache for insightful discussions. Coauthor Dr. James Kossin provided additional data from his 2009 paper with Matt Sitkowi used in Fig. 6 and Table 2. The microwave dataset came from Dr. Christopher Rozoff (Rozoff et al. 2012) and was supplied to us by Dr. Michael Fischer. Dave Vollaro supplied the flight-level data as well as numerous codes to analyze the data. We thank three additional reviewers for their thorough comments and reviews. This work was supported by NSF Grant AGS143311.

#### REFERENCES

- Abarca, S. F., and K. L. Corbosiero, 2011: Secondary eyewall formation in WRF simulations of Hurricanes Rita and Katrina (2005). *Geophys. Res. Lett.*, **38**, L07802, <https://doi.org/10.1029/2011GL047015>.
- , and M. T. Montgomery, 2013: Essential dynamics of secondary eyewall formation. *J. Atmos. Sci.*, **70**, 3216–3230, <https://doi.org/10.1175/JAS-D-12-0318.1>.
- , and —, 2015: Are eyewall replacement cycles governed largely by axisymmetric balance dynamics? *J. Atmos. Sci.*, **72**, 82–87, <https://doi.org/10.1175/JAS-D-14-0151.1>.
- , —, S. A. Braun, and J. Dunion, 2016: On the secondary eyewall formation of Hurricane Edouard (2014). *Mon. Wea. Rev.*, **144**, 3321–3331, <https://doi.org/10.1175/MWR-D-15-0421.1>.
- Bender, M. A., 1997: The effect of relative flow on the asymmetric structure in the interior of hurricanes. *J. Atmos. Sci.*, **54**, 703–724, [https://doi.org/10.1175/1520-0469\(1997\)054<0703:TEORFO>2.0.CO;2](https://doi.org/10.1175/1520-0469(1997)054<0703:TEORFO>2.0.CO;2).
- Braun, S. A., M. T. Montgomery, and Z. Pu, 2006: High-resolution simulation of Hurricane Bonnie (1998). Part I: The organization of eyewall vertical motion. *J. Atmos. Sci.*, **63**, 19–42, <https://doi.org/10.1175/JAS3598.1>.
- Cecil, D. J., E. J. Zipser, and S. W. Nesbitt, 2002: Reflectivity, ice scattering, and lightning characteristics of hurricane eyewalls and rainbands. Part I: Quantitative description. *Mon. Wea. Rev.*, **130**, 769–784, [https://doi.org/10.1175/1520-0493\(2002\)130<0769:RISALC>2.0.CO;2](https://doi.org/10.1175/1520-0493(2002)130<0769:RISALC>2.0.CO;2).
- Corbosiero, K. L., and J. Molinari, 2002: The effects of vertical wind shear on the distribution of convection in TCs. *Mon. Wea. Rev.*, **130**, 2110–2123, [https://doi.org/10.1175/1520-0493\(2002\)130<2110:TEOVWS>2.0.CO;2](https://doi.org/10.1175/1520-0493(2002)130<2110:TEOVWS>2.0.CO;2).
- , —, A. R. Aiyer, and M. L. Black, 2006: The structure and evolution of Hurricane Elena (1985). Part II: Convective asymmetries and evidence for vortex Rossby waves. *Mon. Wea. Rev.*, **134**, 3073–3091, <https://doi.org/10.1175/MWR3250.1>.
- Dai, Y., S. J. Majumdar, and D. S. Nolan, 2017: Secondary eyewall formation in tropical cyclones by outflow–jet interaction. *J. Atmos. Sci.*, **74**, 1941–1958, <https://doi.org/10.1175/JAS-D-16-0322.1>.
- DeMaria, M., 1996: The effect of vertical shear on TC intensity change. *J. Atmos. Sci.*, **53**, 2076–2087, [https://doi.org/10.1175/1520-0469\(1996\)053<2076:TEOVSO>2.0.CO;2](https://doi.org/10.1175/1520-0469(1996)053<2076:TEOVSO>2.0.CO;2).
- , M. Mainelli, L. K. Shay, J. A. Knaff, and J. Kaplan, 2005: Further improvements to the Statistical Hurricane Intensity Prediction Scheme (SHIPS). *Wea. Forecasting*, **20**, 531–543, <https://doi.org/10.1175/WAF862.1>.

- Didlake, A. C., Jr., and R. A. Houze Jr., 2011: Kinematics of the secondary eyewall observed in Hurricane Rita (2005). *J. Atmos. Sci.*, **68**, 1620–1636, <https://doi.org/10.1175/2011JAS3715.1>.
- , G. M. Heymsfield, P. D. Reasor, and S. R. Guimond, 2017: Concentric eyewall asymmetries in Hurricane Gonzalo (2014) observed by airborne radar. *Mon. Wea. Rev.*, **145**, 729–749, <https://doi.org/10.1175/MWR-D-16-0175.1>.
- Frank, W. M., and E. A. Ritchie, 2001: Effects of vertical wind shear on the intensity and structure of numerically simulated hurricanes. *Mon. Wea. Rev.*, **129**, 2249–2269, [https://doi.org/10.1175/1520-0453\(2001\)129<2249:EOVWSO>2.0.CO;2](https://doi.org/10.1175/1520-0453(2001)129<2249:EOVWSO>2.0.CO;2).
- Gamache, J. F., 1997: Evaluation of a fully three-dimensional variational Doppler analysis technique. Preprints, *28th Conf. on Radar Meteorology*, Austin, TX, Amer. Meteor. Soc., 422–423.
- , and F. Marks, 1995: Comparison of three airborne Doppler sampling techniques with airborne in situ wind observations in Hurricane Gustav (1990). *J. Atmos. Oceanic Technol.*, **12**, 171–181, [https://doi.org/10.1175/1520-0426\(1995\)012<0171:COTADS>2.0.CO;2](https://doi.org/10.1175/1520-0426(1995)012<0171:COTADS>2.0.CO;2).
- Hawkins, J. D., M. Helveston, T. F. Lee, F. J. Turk, K. Richardson, C. Sampson, J. Kent, and R. Wade, 2006: Tropical cyclone multiple eyewall configurations. *27th Conf. on Hurricanes and Tropical Meteorology*, Monterey, CA, Amer. Meteor. Soc., 6B.1, <https://ams.confex.com/ams/27Hurricanes/webprogram/Paper108864.html>.
- Heymsfield, G. M., J. B. Halverson, J. Simpson, L. Tian, and T. P. Bui, 2001: ER-2 Doppler radar investigations of the eyewall of Hurricane Bonnie during the Convection and Moisture Experiment-3. *J. Appl. Meteor.*, **40**, 1310–1330, [https://doi.org/10.1175/1520-0450\(2001\)040<1310:EDRIOT>2.0.CO;2](https://doi.org/10.1175/1520-0450(2001)040<1310:EDRIOT>2.0.CO;2).
- Houze, R. A., Jr., S. S. Chen, B. F. Smull, W.-C. Lee, and M. M. Bell, 2007: Hurricane intensity and eyewall replacement. *Science*, **315**, 1235–1239, <https://doi.org/10.1126/science.1135650>.
- Huang, Y.-H., M. T. Montgomery, and C.-C. Wu, 2012: Concentric eyewall formation in Typhoon Sinlaku (2008). Part II: Axisymmetric dynamical processes. *J. Atmos. Sci.*, **69**, 662–674, <https://doi.org/10.1175/JAS-D-11-0114.1>.
- Jones, S. C., 1995: The evolution of vortices in vertical shear. I: Initially barotropic vortices. *Quart. J. Roy. Meteor. Soc.*, **121**, 821–851, <https://doi.org/10.1002/qj.49712152406>.
- Jorgensen, D. F., 1984: Mesoscale and convective scale characteristics of mature hurricanes. Part I: General observations by research aircraft. *J. Atmos. Sci.*, **41**, 1268–1286, [https://doi.org/10.1175/1520-0469\(1984\)041<1268:MACSCO>2.0.CO;2](https://doi.org/10.1175/1520-0469(1984)041<1268:MACSCO>2.0.CO;2).
- Keptert, J. D., 2013: How does the boundary layer contribute to the eyewall replacement cycles in axisymmetric tropical cyclones? *J. Atmos. Sci.*, **70**, 2808–2830, <https://doi.org/10.1175/JAS-D-13-046.1>.
- , 2017: Time and space scales in the tropical cyclone boundary layer, and the location of the eyewall updraft. *J. Atmos. Sci.*, **74**, 3305–3323, <https://doi.org/10.1175/JAS-D-17-0077.1>.
- Klotz, B. W., and H. Jiang, 2017: Examination of surface wind asymmetries in tropical cyclones. Part I: General structure and wind shear impacts. *Mon. Wea. Rev.*, **145**, 3989–4009, <https://doi.org/10.1175/MWR-D-17-0019.1>.
- Kossin, J. P., and M. Sitkowski, 2009: An objective model for identifying secondary eyewall formation in hurricanes. *Mon. Wea. Rev.*, **137**, 876–892, <https://doi.org/10.1175/2008MWR2701.1>.
- , and M. DeMaria, 2016: Reducing operational hurricane intensity forecast errors during eyewall replacement cycles. *Wea. Forecasting*, **31**, 601–608, <https://doi.org/10.1175/WAF-D-15-0123.1>.
- Mallen, K. J., M. T. Montgomery, and B. Wang, 2005: Reexamining the near-core radial structure of the TC primary circulation: Implications for vortex resiliency. *J. Atmos. Sci.*, **62**, 408–425, <https://doi.org/10.1175/JAS-3377.1>.
- Molinari, J., and D. Vollaro, 2008: Extreme helicity and intense convective towers in Hurricane Bonnie. *Mon. Wea. Rev.*, **136**, 4355–4375, <https://doi.org/10.1175/2008MWR2423.1>.
- , and —, 2010: Rapid intensification of a sheared tropical storm. *Mon. Wea. Rev.*, **138**, 3869–3885, <https://doi.org/10.1175/2010MWR3378.1>.
- Montgomery, M. T., and R. J. Kallenbach, 1997: A theory for vortex Rossby-waves and its application to spiral bands and intensity changes in hurricanes. *Quart. J. Roy. Meteor. Soc.*, **123**, 435–465, <https://doi.org/10.1002/qj.49712353810>.
- Nguyen, L. T., and J. Molinari, 2012: Rapid intensification of a sheared, fast-moving hurricane over the Gulf Stream. *Mon. Wea. Rev.*, **140**, 3361–3378, <https://doi.org/10.1175/MWR-D-11-00293.1>.
- Nolan, D. S., Y. Moon, and D. P. Stern, 2007: Tropical cyclone intensification from asymmetric convection: Energetics and efficiency. *J. Atmos. Sci.*, **64**, 3377–3405, <https://doi.org/10.1175/JAS3988.1>.
- Nong, S., and K. Emanuel, 2003: A numerical study of the genesis of concentric eyewalls in hurricanes. *Quart. J. Roy. Meteor. Soc.*, **129**, 3323–3338, <https://doi.org/10.1256/qj.01.132>.
- Pendergrass, A. G., and H. E. Willoughby, 2009: Diabatically induced secondary flows in tropical cyclones. Part I: Quasi-steady forcing. *Mon. Wea. Rev.*, **137**, 805–821, <https://doi.org/10.1175/2008MWR2657.1>.
- Rappaport, E. N., and Coauthors, 2009: Advances and challenges at the National Hurricane Center. *Wea. Forecasting*, **24**, 395–419, <https://doi.org/10.1175/2008WAF2222128.1>.
- Reasor, P. D., and M. D. Eastin, 2012: Rapidly intensifying Hurricane Guillermo (1997). Part II: Resilience in shear. *Mon. Wea. Rev.*, **140**, 425–444, <https://doi.org/10.1175/MWR-D-11-00080.1>.
- , M. T. Montgomery, and L. D. Grasso, 2004: A new look at the problem of tropical cyclones in vertical shear flow: Vortex resiliency. *J. Atmos. Sci.*, **61**, 3–22, [https://doi.org/10.1175/1520-0469\(2004\)061<0003:ANLATP>2.0.CO;2](https://doi.org/10.1175/1520-0469(2004)061<0003:ANLATP>2.0.CO;2).
- , M. D. Eastin, and J. F. Gamache, 2009: Rapidly intensifying Hurricane Guillermo (1997). Part I: Low-wavenumber structure and evolution. *Mon. Wea. Rev.*, **137**, 603–631, <https://doi.org/10.1175/2008MWR2487.1>.
- Riemer, M., M. T. Montgomery, and M. E. Nicholls, 2010: A new paradigm for intensity modification of TCs: Thermodynamic impact of vertical wind shear on the inflow layer. *Atmos. Chem. Phys.*, **10**, 3163–3188, <https://doi.org/10.5194/acp-10-3163-2010>.
- Rogers, R. F., S. S. Chen, J. Tenerelli, and H. E. Willoughby, 2003: A numerical study of the impact of vertical shear on the distribution of rainfall in Hurricane Bonnie (1998). *Mon. Wea. Rev.*, **131**, 1577–1599, <https://doi.org/10.1175//2546.1>.
- , S. Lorsolo, P. Reasor, J. Gamache, and F. Marks, 2012: Multiscale analysis of tropical cyclone kinematic structure from airborne Doppler radar composites. *Mon. Wea. Rev.*, **140**, 77–99, <https://doi.org/10.1175/MWR-D-10-05075.1>.
- , P. D. Reasor, and J. A. Zhang, 2015: Multiscale structure and evolution of Hurricane Earl (2010) during rapid intensification. *Mon. Wea. Rev.*, **143**, 536–562, <https://doi.org/10.1175/MWR-D-14-00175.1>.
- Rozoff, C. M., D. S. Nolan, J. P. Kossin, F. Zhang, and J. Fang, 2012: The roles of an expanding wind field and inertial stability in tropical cyclone secondary eyewall formation. *J. Atmos. Sci.*, **69**, 2621–2643, <https://doi.org/10.1175/JAS-D-11-0326.1>.
- Shelton, K. L., and J. Molinari, 2009: Life of a six-hour hurricane. *Mon. Wea. Rev.*, **137**, 51–67, <https://doi.org/10.1175/2008MWR2472.1>.

- Simpson, R., and R. Riehl, 1958: Mid-tropospheric ventilation as a constraint on hurricane development and maintenance. Preprints, *Tech. Conf. on Hurricanes*, Miami Beach, FL, Amer. Meteor. Soc., D4-1–D4-10.
- Sitkowski, M., J. P. Kossin, and C. M. Rozoff, 2011: Intensity and structure changes during hurricane eyewall replacement cycles. *Mon. Wea. Rev.*, **139**, 3829–3847, <https://doi.org/10.1175/MWR-D-11-00034.1>.
- Tang, B., and K. Emanuel, 2010: Midlevel ventilation's constraint on TC intensity. *J. Atmos. Sci.*, **67**, 1817–1830, <https://doi.org/10.1175/2010JAS3318.1>.
- Terwey, W. D., and M. T. Montgomery, 2008: Secondary eyewall formation in two idealized, full-physics modeled hurricanes. *J. Geophys. Res.*, **113**, D12112, <https://doi.org/10.1029/2007JD008897>.
- Uhlhorn, E. W., B. W. Klotz, T. Vukicevic, P. D. Reasor, and R. F. Rogers, 2014: Observed hurricane wind speed asymmetries and relationships to motion and environmental shear. *Mon. Wea. Rev.*, **142**, 1290–1311, <https://doi.org/10.1175/MWR-D-13-00249.1>.
- Vigh, J. L., and W. H. Schubert, 2009: Rapid development of the tropical cyclone warm core. *J. Atmos. Sci.*, **66**, 3335–3350, <https://doi.org/10.1175/2009JAS3092.1>.
- Wentz, F. J., C. Gentemann, D. Smith, and D. Chelton, 2000: Satellite measurements of sea surface temperature through clouds. *Science*, **288**, 847–850, <https://doi.org/10.1126/science.288.5467.847>.
- Willoughby, H. E., and M. B. Chelmon, 1982: Objective determination of hurricane tracks from aircraft observations. *Mon. Wea. Rev.*, **110**, 1298–1305, [https://doi.org/10.1175/1520-0493\(1982\)110<1298:ODOHTF>2.0.CO;2](https://doi.org/10.1175/1520-0493(1982)110<1298:ODOHTF>2.0.CO;2).
- , J. A. Clos, and M. G. Shoreibah, 1982: Concentric eye walls, secondary wind maxima, and the evolution of the hurricane vortex. *J. Atmos. Sci.*, **39**, 395–411, [https://doi.org/10.1175/1520-0469\(1982\)039<0395:CEWSWM>2.0.CO;2](https://doi.org/10.1175/1520-0469(1982)039<0395:CEWSWM>2.0.CO;2).
- , F. D. Marks Jr., and R. J. Feinberg, 1984: Stationary and moving convective bands in hurricanes. *J. Atmos. Sci.*, **41**, 3189–3211, [https://doi.org/10.1175/1520-0469\(1984\)041<3189:SAMCBI>2.0.CO;2](https://doi.org/10.1175/1520-0469(1984)041<3189:SAMCBI>2.0.CO;2).
- Zhang, F., D. Tao, Y. Qiang Sun, and J. D. Kepert, 2017: Dynamics and predictability of secondary eyewall formation in sheared TCs. *J. Adv. Model. Earth Syst.*, **9**, 89–112, <https://doi.org/10.1002/2016MS000729>.
- Zhang, J. A., R. F. Rogers, P. D. Reasor, E. W. Uhlhorn, and F. D. Marks Jr., 2013: Asymmetric hurricane boundary layer structure from dropsonde composites in relation to the environmental vertical wind shear. *Mon. Wea. Rev.*, **141**, 3968–3984, <https://doi.org/10.1175/MWR-D-12-00335.1>.
- Zhu, T., D.-L. Zhang, and F. H. Weng, 2004: Numerical simulation of Hurricane Bonnie (1998). Part I: Eyewall evolution and intensity changes. *Mon. Wea. Rev.*, **132**, 225–241, [https://doi.org/10.1175/1520-0493\(2004\)132<0225:NSOHBP>2.0.CO;2](https://doi.org/10.1175/1520-0493(2004)132<0225:NSOHBP>2.0.CO;2).
- Zhu, Z., and P. Zhu, 2014: The role of outer rainband convection in governing the eyewall replacement cycle in numerical simulations of tropical cyclones. *J. Geophys. Res. Atmos.*, **119**, 8049–8072, <https://doi.org/10.1002/2014JD021899>.